## POLITECNICO DI TORINO
## Repository ISTITUZIONALE

In situ alloying of AlSi10Mg-5 wt% Ni through laser powder bed fusion and subsequent heat treatment

(Article begins on next page)

01 September 2025

# In situ alloying of AlSi10Mg-5 wt. % Ni through laser powder bed fusion and subsequent heat treatment

**Mohammad Reza Jandaghi** *,[1], **Alberta Aversa** [1], **Diego Manfredi** [1], **Flaviana Calignano** [2], **Luca Lavagna** [1], **Matteo Pavese** [1]

[1] *Department of Applied Science and Technology, Politecnico di Torino, Corso Duca degli Abruzzi 24, 10129 Torino, Italy*

[2] *Department of Management and Production Engineering (DIGEP), Politecnico di Torino, Corso Duca degli Abruzzi 24, 10129 Torino, Italy*

*\*Corresponding author*; *E-mail:* ***mohammadreza.jandaghi@polito.it***

## Abstract

In the current study, the effect of in-situ alloying of AlSi10Mg with 5 wt.% Ni (pseudoeutectic composition) through the LPBF additive manufacturing technique was investigated. Fabricated samples underwent supplementary annealing treatment at 300 °C for 15 and 120 min, eventually. During the thermal treatment, the fish-scale grains created after printing inside the melt pools after printing vanished gradually. In the as-built sample, molten Ni particles settled as big chunks of $Al_3Ni$ in the center and a thin strip of tiny Ni-rich masses in the borders of the melt pools. FIB/SEM and AFM images revealed that after 15 min annealing, silicon cellular dendrites fragment into fine Si particles, and during annealing for 120 min, the aluminium matrix expels out the supersaturated solute silicon atoms. Consequently, Si atoms leave the substrate and diffuse to pre-existing Si particles in cell walls and the triple junctions. Such a collective diffusion of Si atoms leads to the formation of coarse Si particles widespread in the Al matrix. Based on the XRD outputs, annealing for 15 min had not any major effect on Ni-rich phases. however after 120 min, a more brittle intermetallic shell of a Ni-rich phase formed on pre-exist coarse phases. The comparison of the mechanical properties of the Ni-reinforced AlSi10Mg alloy with those reinforced via the addition of other elements/compounds revealed that in a size range close to AlSi10Mg particles, Ni could not be an appropriate candidate for in-situ alloying through the LPBF method. Furthermore, spheroidization of the silicon particles and formation of fragile Ni-rich intermetallic shells having weak interfacial bonding to the Al matrix during the long-term annealing results in a significant reduction in mechanical strength of the specimens.

*Keywords: Additive manufacturing; Laser Powder Bed Fusion (LPBF); Al10SiMg; Microstructure; Mechanical properties; Annealing.*

# 1. Introduction

In recent years, Laser Powder Bed Fusion (LPBF), one of the emerging additive manufacturing (AM) technologies, has been extensively adopted to fabricate geometrically complex-shape components and lightweight structures, particularly in aerospace and automotive industries. This technique allows the production of parts with shapes that cannot be produced by other conventional methods such as machining, forming, welding, and casting. LPBF is a term that the ASTM has introduced to refer to the technique that is often known as Selective Laser Melting (SLM) or Direct Metal Laser Sintering (DMLS) [1, 2]. During the LPBF process, three-dimensional (3D) objects are fabricated through a layerwise process starting from a layer of powder which is spread on a building platform and then melted selectively using a laser source that follows a computer-aided design (CAD) data [3]. It is well documented that owing to the rapid solidification during the LPBF process (estimated cooling rate lies between $10^4$ and$10^6$ K/s), the formation of an ultrafine microstructure and consequently higher mechanical strength can be expected [4]. Hence, the LPBF technique offers the possibility of further improvement of the strength-to-weight ratio of aluminium alloys [5].

AlSi10Mg alloy is one of the most investigated alloys processed via the LPBF method [6]. This high level of interest originated from its low melting point and thermal expansion, low susceptibility to solidification cracking as well as good weldability. In addition, the chemical composition of this alloy which is near the eutectic composition, makes it easy processable through laser-based technologies [7, 8]. Moreover, AlSi10Mg belong to the ageing/precipitate hardenable alloys that can reach higher strength when subjected to a specific supplementary heat treatment [9]. For instance, Maamoun et al. [10] and Aboulkhair et al. [11] surveyed the effect of annealing on the structure and mechanical properties of AlSi10Mg. Their outcomes indicated that despite short-term annealing (1-5 h), T6 heat treatment can significantly enhance the hardness of this alloy due to the formation of $Mg_2Si$ and $Al_5FeSi$ precipitates. Previous researchers [12-14] declared that annealing temperature plays an effective role in the size of the Si particles, and solution treatment below the standard T6 temperature (550 °C) eventuates in finer Si particles and guarantees higher mechanical strength. Kimura et al. [15] revealed that complete disassociation of Si dendritic structure occurs after a long-term solution treatment over 300 °C.

Furthermore, many efforts have been made to improve the mechanical properties of AlSi10Mg alloy through the addition of grain refiners like $LaB_6$ [16] and BN [17]. However, only some of

them were slightly effective, while most of them could not remarkably improve the mechanical strength. Another approach that has been reported so far to improve the mechanical strength of AlSi10Mg alloy is the addition of reinforcing particles to produce AlSi10Mg based composites [18]. For instance, $TiB_2$ [19, 20], graphene [21], CNT [22], and TiC [23-25] were found to be promising reinforcements for AlSi10Mg alloy. However, it is well reported that in most of the cases, the interfacial bonding between the Al matrix and reinforcements is rather weak, and consequently, this weak point degrades the mechanical performance of the sample [26, 27]. Another approach that can be effective to improve the mechanical strength of the AlSi10Mg alloy is a slight modification of its chemical composition that can be implemented through the in-situ alloying process. Nevertheless, based on the authors' knowledge, far too little attention has been paid to the development of new AlSi10Mg alloys through the in-situ alloying process. Hence, the aim of this work is at first to assess the feasibility of producing Ni-modified AlSi10Mg alloy through the LPBF method. The second target in this research is to evaluate the impact of thermal post-processing on the microstructure and mechanical properties of the newly developed alloy. In this regard, the microstructure and phase transformations linked to the addition of nickel were analyzed carefully and their correlation with tensile strength and fracture mechanism of the samples was elucidated.

## 2- Experimental procedures

### 2.1. Materials

To prepare the feedstock materials a gas atomized AlSi10Mg powder (supplied by EOS GmbH) sieved under 45 μm was mixed with 5 wt. % atomized Ni powder (supplied by Sigma Aldrich Co.) with a size range below 20 μm. The size distribution histogram of the mixed powder is presented in Fig. 1. The size of the Ni powder was chosen fine enough to facilitate their complete melting and ensure the homogeneity of the chemical composition all over the sample. However, due to the significant difference between the melting point of Ni (1455 °C) and AlSi10Mg (near 570 °C), optimization of the building parameters would be very critical. Likewise, this proportion was chosen close to the eutectic point to reduce the solidification cracking possibility. The chemical composition of the used powder determined by Energy

Dispersive Spectroscopy (EDS) analysis is given in **Table 1**. The elemental distribution map analysis of the as-mixed AlSi10Mg/Ni powder, shown in **Fig. 2,** adequately confirms that the Ni particles were distributed uniformly within the AlSi10Mg powder.
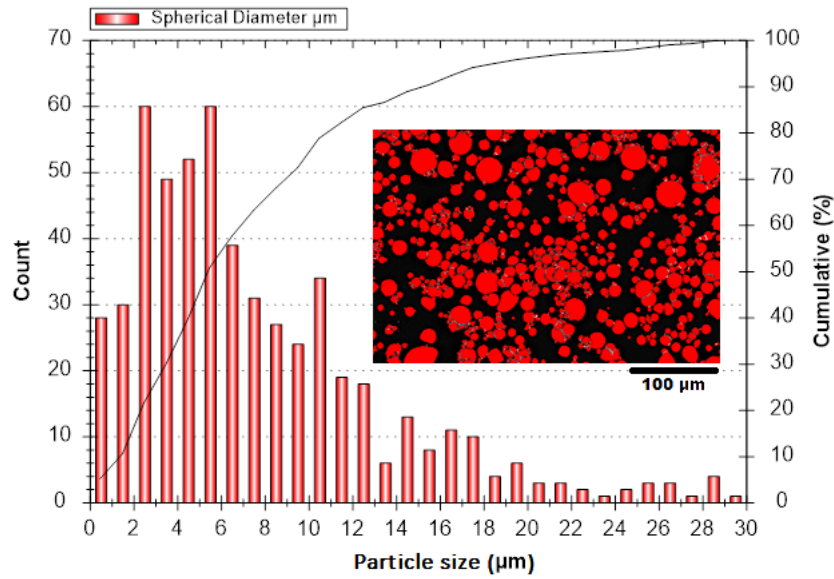


**Fig. 1**. The particle size distribution of the prepared AlSi10Mg+5%Ni powder.

**Table 1.** Chemical composition by EDS of the mixed powder

| Element | Al | Si | Mg | Mn | Ti | Cu | Ni |
|---|---|---|---|---|---|---|---|
| AlSi10Mg+Ni | Bal. | 8.5-10.5 | 0.18-42 | <0.55 | <0.15 | <0.05 | 5.1 |
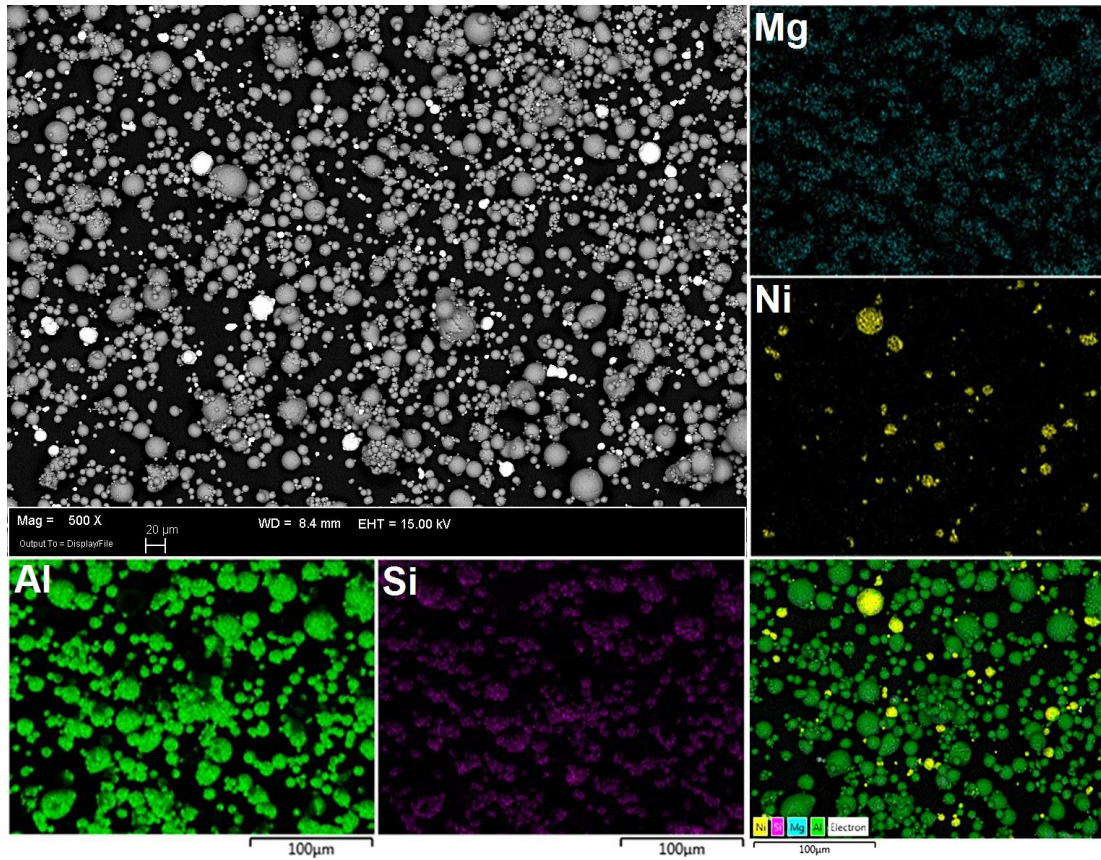
**Fig. 2**. Elemental distribution map of the prepared AlSi10Mg+5%Ni powder.

## 2.2. Sample production

The specimens were printed using an EOS M270 system (maximum power, 200 W; beam spot diameter, 100 μm; laser wavelength, 1060-1100 nm) with the optimum process parameters identified in an earlier study [28]. The building process was executed under a flowing inert high purity Ar atmosphere, with the oxygen level kept below 0.1%, while the temperature of the building platform was 100 °C. The as-prepared specimens were annealed at 300 °C for 15 min and 120 min and air-cooled eventually. In order to trace the phase evolutions in higher temperatures by XRD, one sample annealed at 400 °C for 120 min.

## 2.3. Characterization and mechanical evaluation

All samples for microstructural investigation were cut along the building direction (BD) and mechanically ground and polished using SiC papers (1200, 2500 and 4000 grit size) and diamond suspension, respectively. In the following, as-polished surfaces were electro-etched using JE-WorldTech patented etchant [29] for optical analysis and chemically etched using Keller's solution for SEM analysis. The optical microstructure of the samples was

characterized by a Leica DMI5000 M microscope. A ZEISS Supra 40 Field Emission Scanning Electron Microscopy (FE-SEM) equipped with an Oxford EDS microanalysis (Liquid-N2 cooled Si(Li) detector and Helios NanoLab 600i Dual-Beam focused ion beam scanning electron microscopy (FIB-SEM) equipped with 4 gas injection systems for deposition (Pt, Au, $SiO_x$) and etching ($XeF_2$) were employed for detecting the evolution of the particles. In order to trace the surface topography, Atomic Force Microscopy (AFM) was employed. Phase transformations were analyzed by X-ray diffraction (XRD) using a X-Pert Philips diffractometer in a Bragg Brentano configuration in a $2\theta$ range between 10 and 110° (operated at 40 kV and 40 mA by a step size 0.013 and 25 s per step).

Samples for the tensile test were machined according to ASTM E8 Standard **[30].** The tensile tests were carried out at room temperature using an Zwick/Roell Z050 testing machine with a 2 mm/min crosshead velocity. The presented data are the average of at least three specimens processed using similar conditions to ensure the reproducibility of the results.

## 3. Results and Discussion

### 3.1. *Microstructural characterization*

The 3D micrograph of an as-built sample, shown in **Fig. 3(a)**, reveals the melt pools orientation along the BD and laser traces on the top surface. **Figs. 3b** and **3c** adequately show the different phase evolutions in the center and border of the melt pools. According to these images, the interface of the melt pools comprises a coarse dendritic silicon structure with varying thicknesses. Likewise, the Marangoni effect appears as a circular flow inside some of the melt pools.
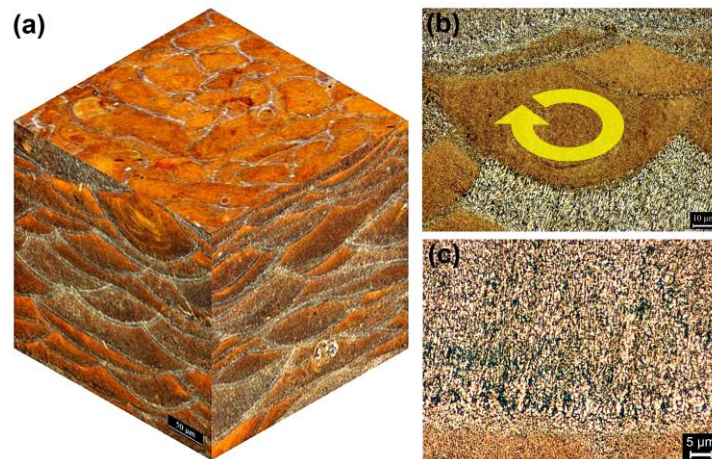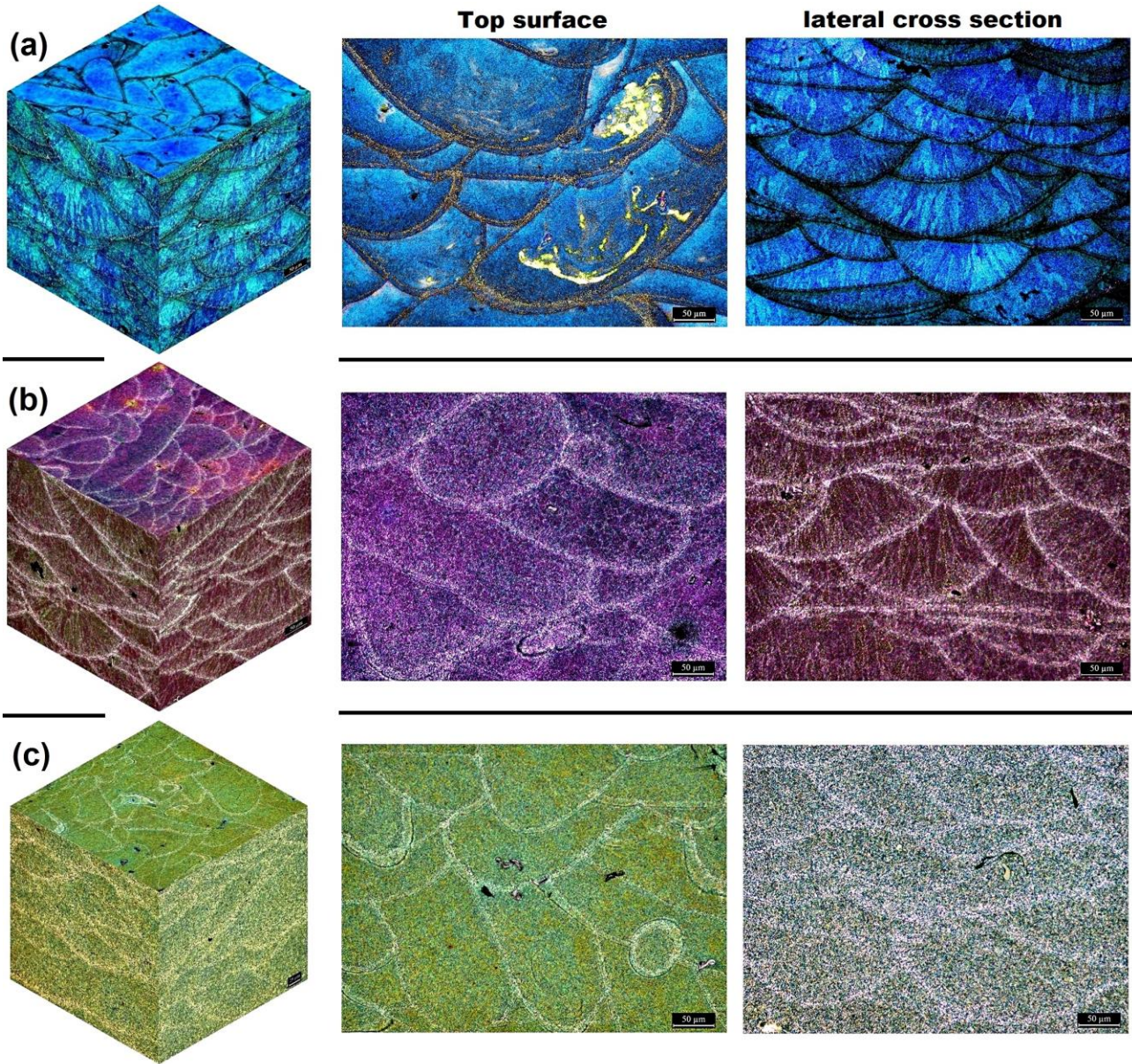
**Fig. 3.** Microstructure of an as-built sample in (a) 3D view and cross-section (b,c) in two different magnifications.

The optical micrographs of the AlSi10Mg/Ni samples after short-term and long-term annealing are displayed in **Fig. 4**. Based on **Fig 4(a)**, the as-built specimen comprised the elongated grains perpendicular to the melt pool boundaries due to the Gaussian distribution of the laser beam energy **[31]**. Epitaxial grain growth that generally results in the formation of elongated columnar grains in an individual melt pool and an overall zigzag pattern along the BD is a typical phenomenon in the LPBF fabricated samples **[32]**. It is well documented that this epitaxial grain growth originates from directional solidification in the reverse direction to the heat transfer in LPBF manufactured parts.

According to the top surface image of the as-built sample, some Ni-rich phases are pushed to the fusion borders. Likewise, some unmelted phases are stacked inside the melt pools. Accumulation of these phases in the melt pool borders, in turn, contributes to the formation of elongated grains from the borders toward the center of the melt pools. In general, it is reported that the $G/R$ ratio at the solid-liquid interface ($G$ and $R$ are the thermal gradient and solidification rate, respectively) is the key solidification parameter in the formation of specific grain morphologies in different regions of a sample **[33]**. As this value decreases, planar, cellular, columnar dendritic, and equiaxed dendritic structures can be formed, respectively **[7]**. Therefore, when Ni phases settle in the melt pool boundaries, many small grains can heterogeneously nucleate at the borders due to the large value of G. Owing to the high magnitude of G/R, most of the nucleated grains on borders compete to grow as columnar grains, whereas few of them can grow towards the center of the melt pool.

**Fig. 4(b)** shows the microstructure of the as-built sample after annealing for 15 min at 300 °C. As can be seen, the morphology and size of the grains are still stable and have not significantly changed. The fine grains on the top surface of the sample are cross-sections of elongated grains along the building direction. According to **Fig. 4(c)**, by annealing over 120 min at 300 °C, the fish scale pattern has almost vanished, and the melt pool boundaries gradually merged. Furthermore, despite annihilating the grain structure after long-term annealing, the phases formed in the borders did not leave their initial location completely and appeared with different contrast.

**Fig. 4**. LOM microstructure of the (a) as-built sample and after annealing at 300 °C for 15 min (b) and 120 min (c).

To better assess the structural transition in the as-built samples during annealing, FIB/SEM imaging was employed at different magnifications, and the results are presented in **Fig. 5**. According to **Figs. 5(a,b)**, in the as-built specimen, a network of interconnected silicon dendrites is widespread in the supersaturated α-Al matrix. After 15 min treatment at 300 ℃, most of the linkages between eutectic Si cellular structure were detached, and the conjunct silicon phases were dissociated into the ultrafine particles (**Figs. 5c** and **5d**). As the annealing time increases, supersaturated α-Al tends to repulse the excessive dissolved silicon into the matrix and reach a stable thermomechanical condition. In the following, by diffusion and

agglomeration of silicon into the spheroidized precipitated phases due to Ostwald ripening phenomenon [2, 25], fine particles became coarser and significantly reduced their number (Figs. 5e and 5f). During this thermodynamically driven spontaneous phenomenon, to reduce the lattice stored energy, the less-stable atoms located on the surface of the smaller particles diffuse to the larger ones with higher volume to surface proportion. Consequently, the smaller particles gradually shrink and/or coalesce to form bigger particles.
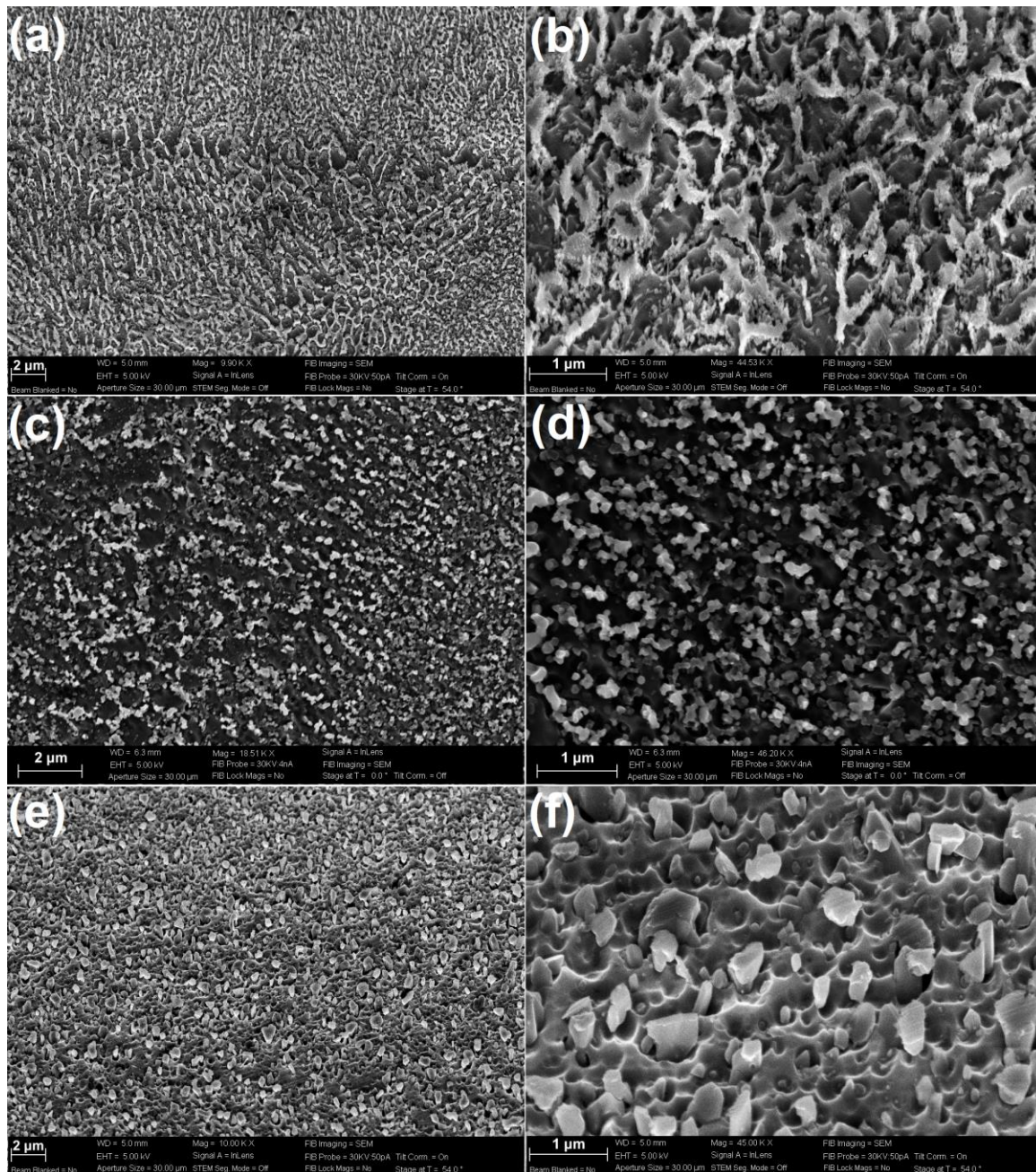


**Fig. 5**. FIB/SEM micrograph of the (a,b) as-built sample and after annealing at 300 °C for 15 min (c,d) and 120 min (e,f).

The acquired evidence after topography analysis of the surface through the AFM analysis validated the FIB/SEM results (**Fig. 6**). As shown in the as-built sample, the walls of the cellular dendrites are composed of delicate needle silicon particles, while triple junctions contain coarser silicon particles (**Fig. 6a-c**). According to the literature, triple junctions have higher stored energy, and during the thermal treatments, they start to melt at a temperature below the standard melting point **[34-37]**. Since the cell walls are indeed the sub-grain boundaries, probably higher diffusion kinetics has led to partial coarsening of the silicon particles in the triple junctions (**Fig. 6c**). These coarse particles can be the destination of the migrated solute atoms of silicon when leaving the supersaturated Al matrix during the heat treatment process. Consequently, after annealing at 300 °C for 120 min, numerous coarse silicon particles were uniformly distributed in silicon-free Al matrix (**Fig. 6(d,e)**).
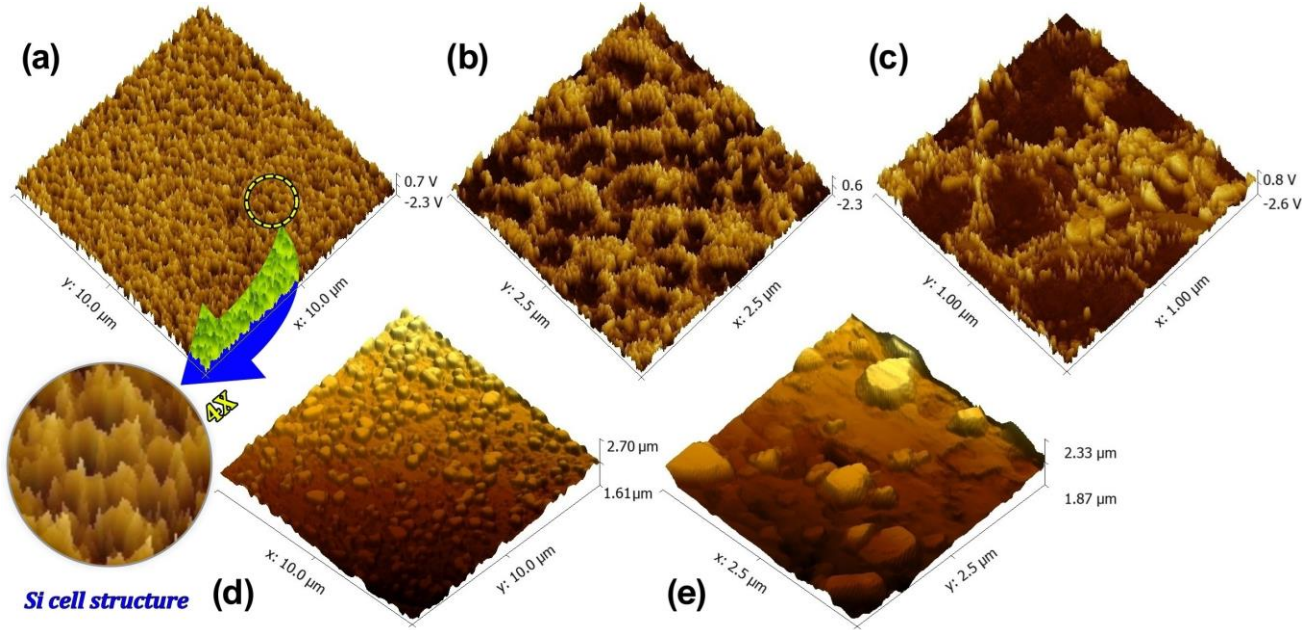


**Fig. 6.** AFM images show the cross-section of the as-built sample (a-c) after annealing at 300 °C for 120 min (d,e).

Exposure to different thermal treatments leads to the formation of three different zones in terms of morphology and size of the cellular dendrites across the melt pools (**Fig. 7a**). The fine zone (MP fine) in which the size of the cellular dendrites does not exceed 500 nm **[7, 38]**. The grains in MP fine zone are partially oriented toward the center of the melt pool. The coarse zone at the melt pool border (MP coarse), which has more equiaxed cells with bigger size (2-3 times) compared to the fine area due to a partial remelting and subsequent heat accumulation

at the bottom of the melt pool and symmetrical growth of the cells **[39, 40]**. The third batch of the dendrites is in the Heat Affected Zone (HAZ) that forms on the outskirt of the melt pool below the MP coarse strip. This layer is where during melting of the last deposited powder bed, laser penetration depth was not sufficiently high to remelt it and only was exposed to a temperature between 280-560 °C below a second. Although this temperature was not sufficiently high to propel the long-range diffusion of solute Si to contribute to the particle coarsening there, but the heat transfer of the laser could fragment the Si cellular dendrites. During annealing at 300 °C, the cellular walls gradually collapsed and broke into equiaxed particles. Consequently, after 15 min exposure to this temperature, in fine-grain regions disintegrated Si networks were decorated like the HAZ strip (**Fig. 7b**). As exhibited in **Fig. 7(c)**, the size of the silicon particles upon fragmentation of silicon dendrites and nucleation of new particles from supersaturated Al matrix was in nanoscale. It was proved that the center of the melt pools that benefits from interconnected silicon cells shows higher hardness compared to the borders while HAZ displays the minimum hardness value **[5]**. Hence, regardless of Ni addition and related transformations under thermal treatment, complete dissociation of Si cellular dendrites after annealing, in turn, can reduce the mechanical strength of this alloy.
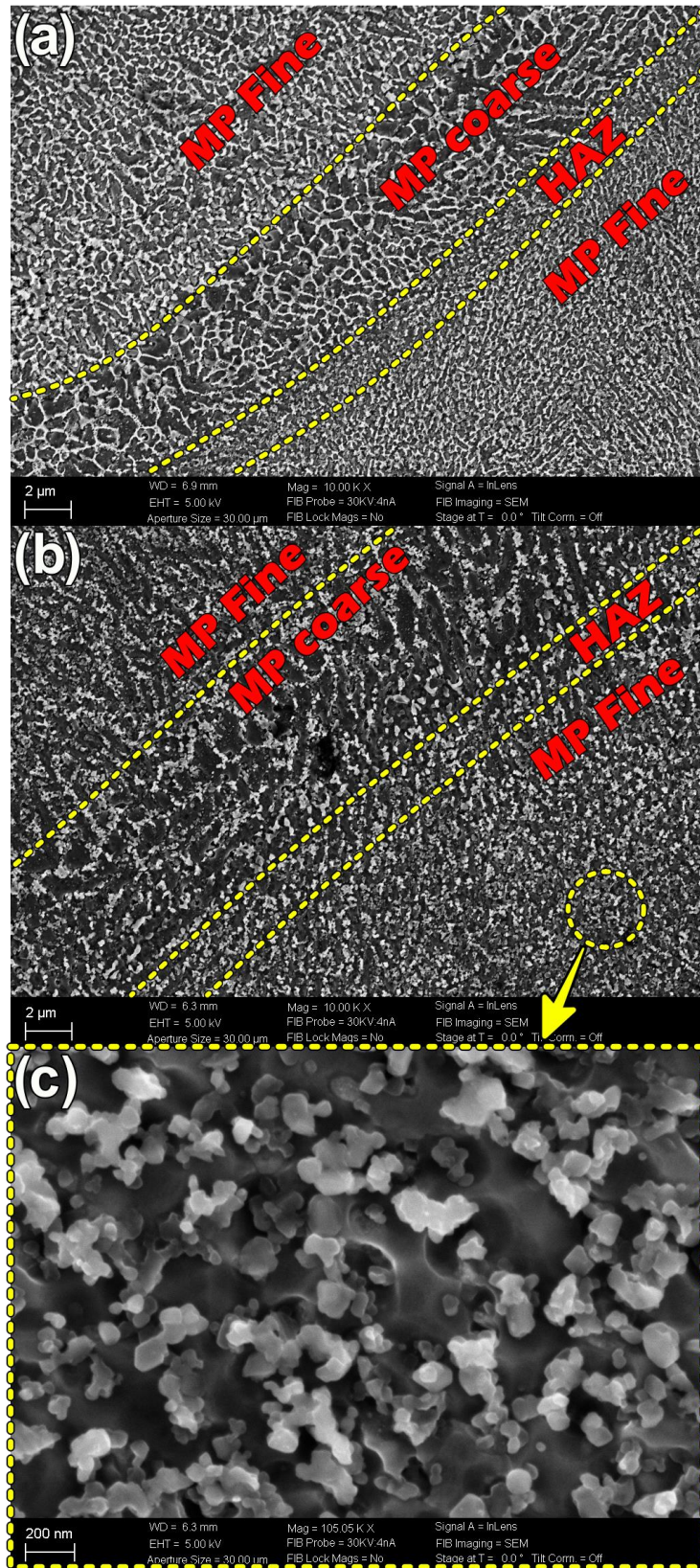
**Fig. 7**. SEM micrographs of the as-built sample (a) after 15 min annealing at 300 °C (b) and formation of the silicon nanoparticles in the fine-grained zone after annealing at 300 °C for 15 min (c).

The elemental distribution map of **Fig. 8 (a-d)** properly shows that during solidification of a new layer, a significant portion of the Ni particles was driven to the melt pool boundaries and stacked there as Ni-rich streaks (similar to **Fig. 4a**). Despite the gradual breakdown of the Si dendrites during annealing at 300 °C for 15 min (**Figs. 8(e-h)**) and 120 min (**Figs. 8(i-l)**), Ni-rich intermetallics were not majorly affected by heat treatment and preserved their initial locations in melt pool boundaries. Comparison of **Figs. 8(c)**, **8(g)** and **8(k)** revealed that during annealing, supersaturated silicon atoms leave the Al matrix and form individual particles or precipitate on pre-existing particles and coarsened them. As a result, gradually, the Al substrate was depleted from the solute silicon atoms, and after 120 min most of the coarsened Si particles were surrounded by the Al atoms.
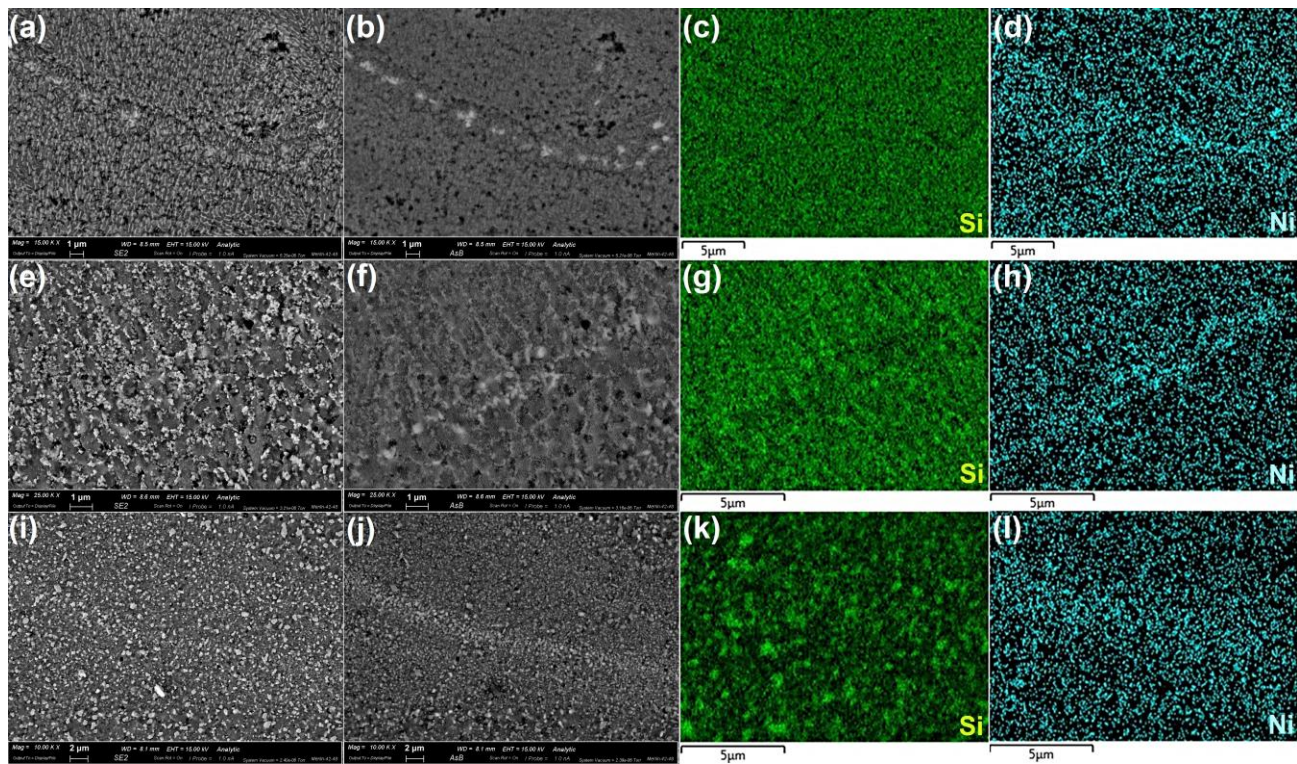


**Fig. 8**. Secondary and backscatter SEM images and distribution map of Si and Ni elements in the as-built sample (a-d), and after annealing at 300 °C for 15 min (e-h) and 120 min (i-l).

Line-scan patterns of **Fig. 9** were taken perpendicular to the melt pool borders after short-term and long-term annealing. Accordingly, differently from the spheroidization of the silicon dendrites and coarsening of the silicon particles through the atomic diffusion from the supersaturated Al matrix, Ni-rich phases are thermodynamically stable up to 300 °C. These

results show that the atoms belonging to Ni lumps could not undergo a long-range diffusion in the Al matrix even after 120 min annealing.
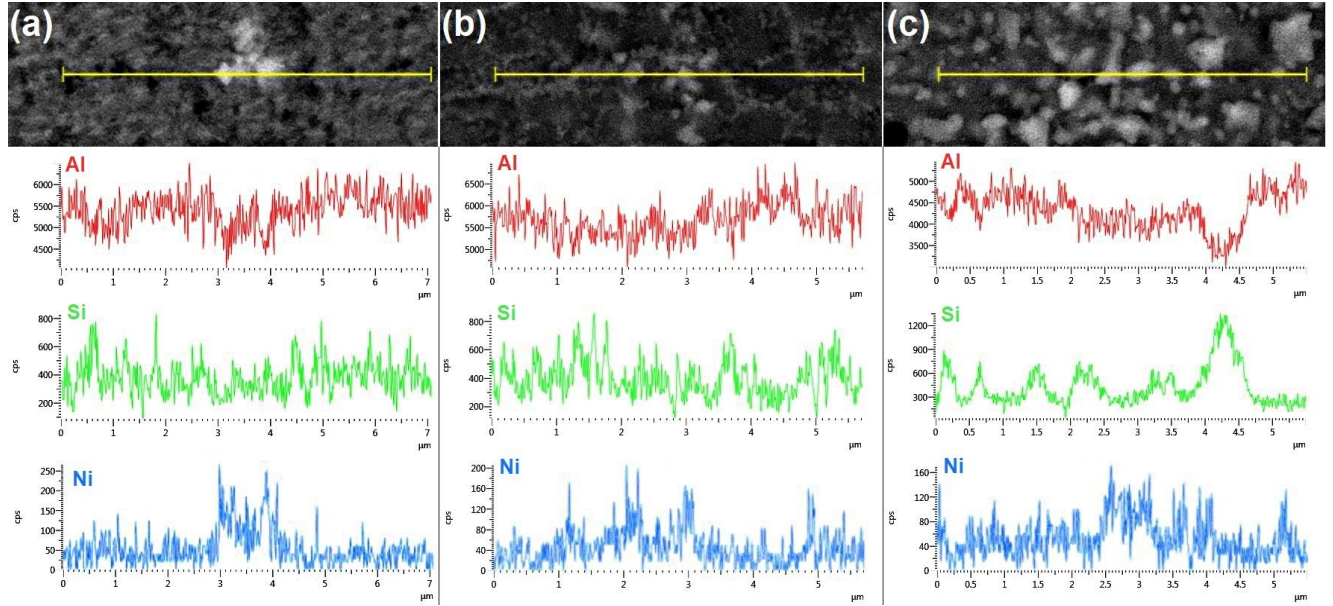


**Fig. 9.** EDS line scan perpendicular to the melt pool boundaries in (a) as-built sample after annealing at 300 °C for 15 min (b) and 120 min (c).

**Fig. 10** shows the destructive role of Ni-rich intermetallics stacked at the melt pool boundaries. As depicted in **Fig. 10(a)**, the accumulation of the molten nickel particles does not limit to the melt pool borders, and some Ni-rich phases were formed at the center of melt pools. Nonetheless, owing to the weakness of the melt pool borders at the interface of MP coarse and HAZ **[41]**, precipitation of the Ni-rich phases made the borders drastically unstable (**Fig. 10(b)**). Consequently, even thermal shock during rapid solidification of the fused layers can cause the crack initiation at melt pool borders and spontaneous failure of the specimen (**Fig. 10(c)**).
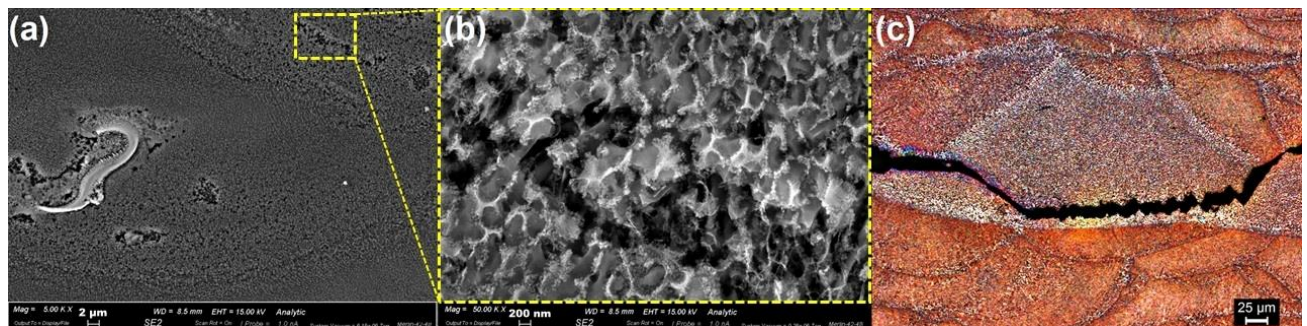


**Fig. 10.** SEM images of stacked Ni-rich phases at the center (a) and melt pool borders (b) and OM micrograph showing the spontaneous failure of the as-built sample from melt pool boundary.

The XRD patterns of **Fig. 11** represent the phase evolutions during short-term and long-term annealing of Ni-reinforced specimens. As shown in the as-built sample, the high temperature of the laser irradiation could melt most of the Ni particles and make a reaction between the molten Ni and aluminium matrix. Consequently, Ni is transformed into $Al_3Ni$ intermetallic chunks. As shown, annealing at 300 °C for 15 min had no influence neither on the AlSi10Mg matrix nor on $Ni_3Al$ phases formed in the printing step. Annealing at 300 °C for 120 min pulled the trigger of reactivity between the present Ni in the substrate as unmelted particles or coarse $Ni_3Al$ chunks with surrounded Al atoms. Consequently, the peak intensity of the $Ni_3Al$ phase is rather intensified. In order to trace the probable further phase evolutions, long-term annealing at a higher temperature also was examined. As can be seen, annealing at 400 °C for 120 min has enhanced the intensity of the $Al_3Ni$ and Si peaks in the XRD pattern of the specimens. It shows that annealing at a higher time and temperature however would increase the reactivity of the Ni-rich phases, but accompanies by dissociation of the Si branches formed during the LPBF process and migration of the Si from supersaturated Al matrix toward the pre-exist Si particles and eventually formation of coarse brittle Si particles.
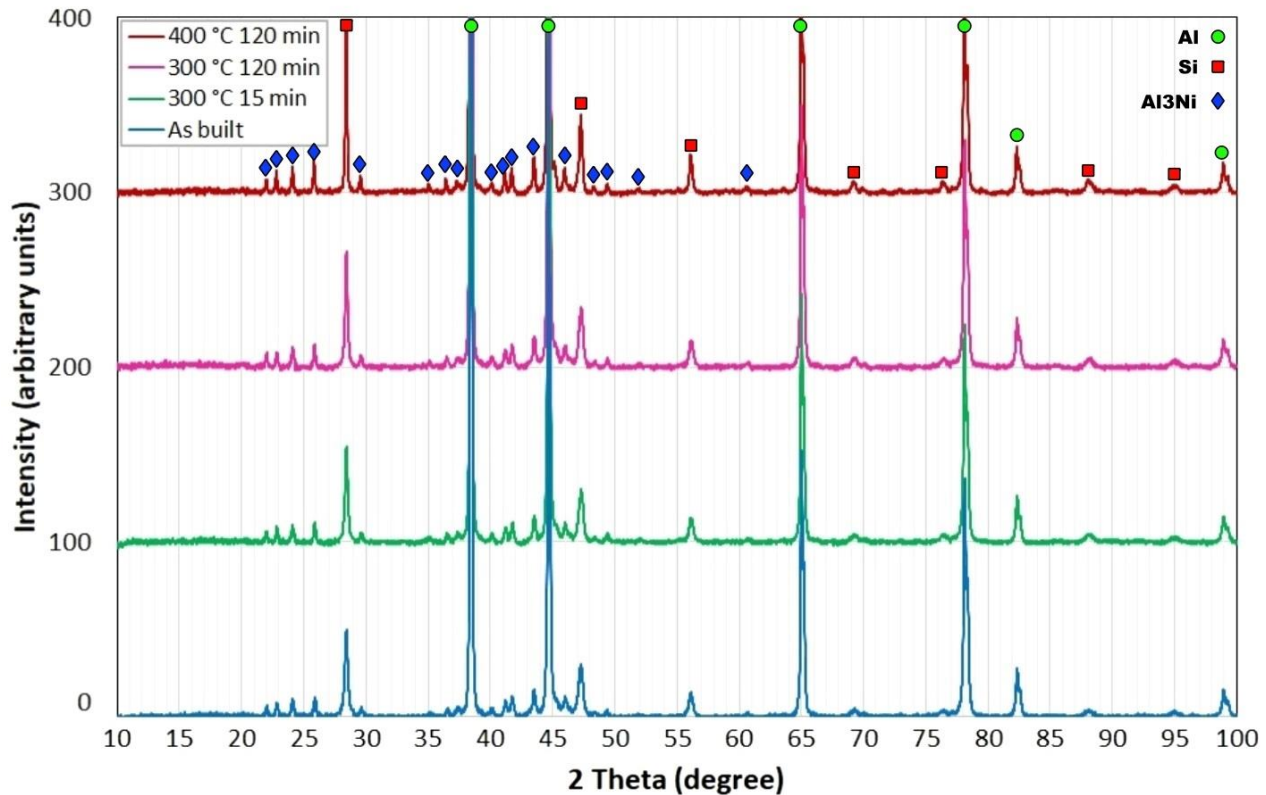


**Fig. 11**. XRD pattern of the as-built specimen after annealing at 300 °C for 15 min and 120 min and 400 °C for 120 min.

**Fig. 12** shows the effect of annealing at 300 °C for 120 min on residual Ni-rich phases. According to the optical micrograph of **Fig. 12(a)**, which is taken from the as-built sample, the chemical composition of coarse Ni-rich chunks is not uniform from surface to center of these regions. It seems that however the heat of laser has evolved most of the Ni particles into $Ni_3Al$ masses, but still the center of these chunks is composed of unreacted Ni. In the following, after 120 min heat treatment at 300 °C, a thin layer of another intermetallic phase has formed around them (**Fig. 12(b)**). The formation of such a thin shell of intermetallic compounds on the Ni-rich lumps implies that despite the destructive influence of Long-term annealing on dendritic silicon structure, it had a slight effect on aggregated Ni-rich phases. However, even after the formation of this shell, the center of the Ni-rich zones remained as unreacted (brown stripe). Regarding the difference between the melting point of AlSi10Mg and Ni (570 °C and 1455 °C), the size range of Ni particles must be considerably smaller to achieve a uniform distribution of $Ni_3Al$ intermetallic particles in the Al substrate. **Figs. 12(c)** and **12(d)** are provided from the fracture surface of the as-built sample and annealed sample at 300 °C for 120 min, respectively. Likewise, EDS analysis of **Figs. 12(e)** and **12(f)**, are related to the exhibited phases in the fracture surface of these two samples. As can be seen, the stacked white phase of **Fig. 12(c)** is enriched from Ni, while a thin gray layer of intermetallic is formed on it. After long-term annealing, a dark crust of intermetallic was formed on it. The smooth surface of this phase is representative of its weak adhesion to the matrix and easy separation under tensile loading. In the meantime, the formation of some cracks on this intermetallic shell points to the brittle nature of this phase.
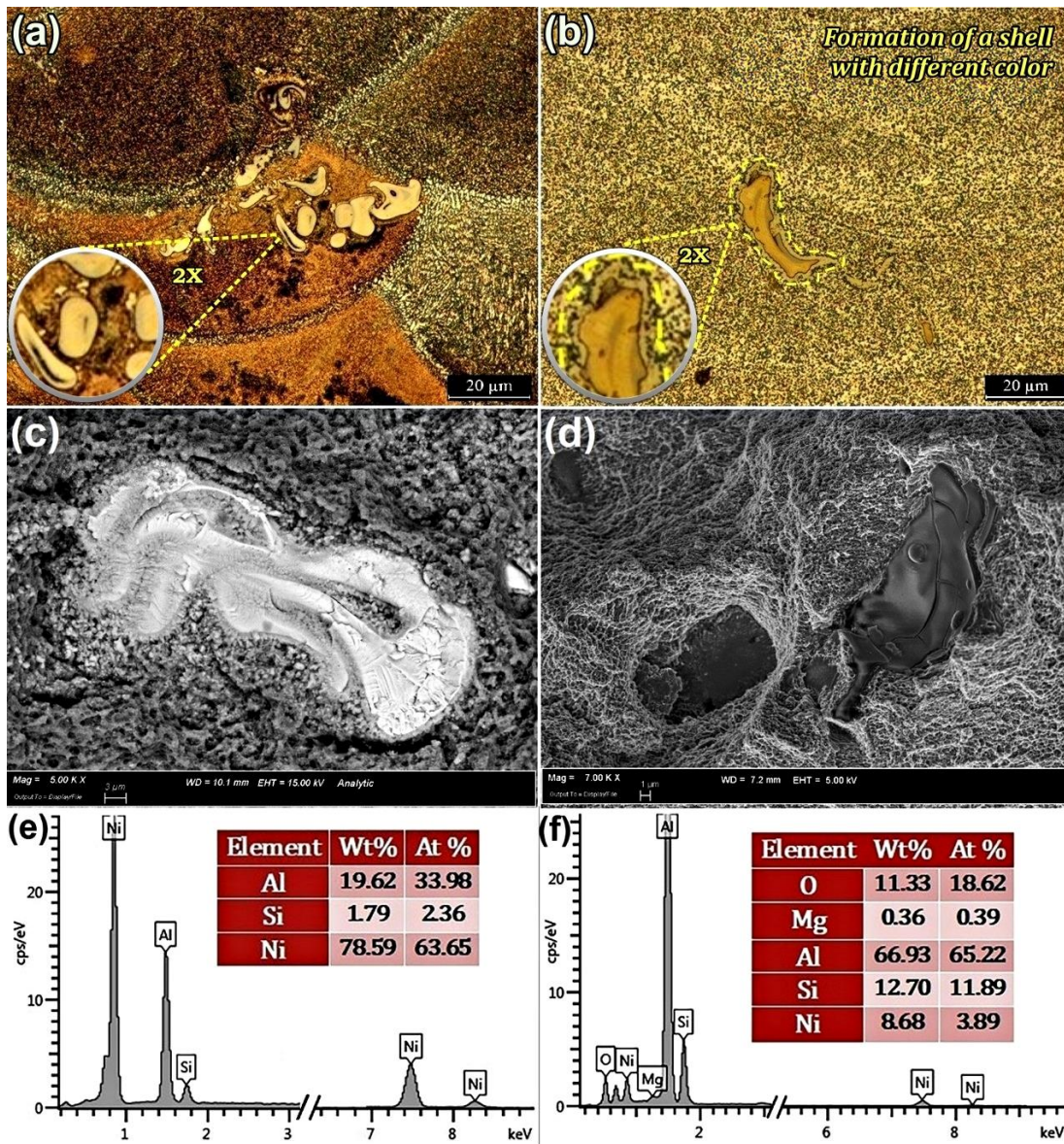
**Fig. 12**. Optical micrograph, SEM image of the fracture surface and EDS analysis of the accumulated phases in the fracture surface of as-built (a, c, e) and annealed samples at 300 °C for 2h (b, d, f).

The elemental distribution map of **Fig. 13**, referring to an as-built specimen, also confirms the presence of coarse Ni-rich chunks in the fracture surface of the as-built specimen. As depicted by arrows, many cracks are formed at the interface of Ni-rich lumps with the aluminium matrix. It can be attributed to the difference in thermal expansion coefficient between Al and the thin intermetallic crusts formed on Ni-rich lumps that detach from the matrix during rapid solidification of the fused layers and act as a failure initiation point during the tensile test.
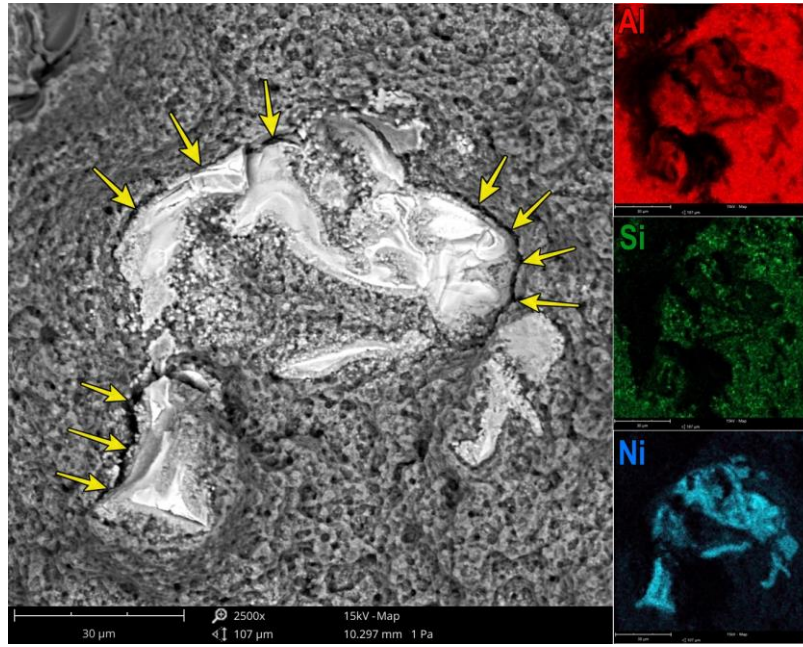
**Fig. 13.** Element distribution map of the aggregated Ni-rich mass in fracture surface of the as-built specimen.

Nonetheless, Ni-rich chunks were not the only origin of the failure under tensile loading. In order to analyze the fracture mechanism in the samples, the fracture surface of the as-built specimen (**Fig. 14 (a-c)**) and of the ones annealed at 300 °C for 120 min (**Fig. 14 (d-f)**) was investigated by stereomicroscope and SEM. According to **Fig. 14 (a, b)**, coarse Ni-rich lumps are uniformly distributed in the fracture surface of the as-built sample and play the main role in the formation of coarse dimples. Likewise, poor metallurgical bonding between the $Ni_3Al$ and Al matrix induced the lack of fusion imperfection (**Fig. 14 (c)**). The spherical hole of **Fig. 14(d)** shows that some gas bubbles were also entrapped inside the melt pools during LPBF printing of the samples. Such a round shape pores having smooth inner walls often form in the center of melt pools. Because regardless of the origin of the gas entrance in the molten pool, namely as evaporation of smaller Al particles by a high laser energy density, hollow powders or absorbed gas from the ambient atmosphere around the melt pool, rapid solidification does not allow it to escape from the molten phase **[42]**. **Figs. 14 (e, f)** shows the high magnification SEM images of the finer dimples in the fracture surface of the long-term annealed specimen. The settlement of the spheroidized silicon particles at the bottom of the fine dimples shows that these fine irregular shape particles can also act as crack nucleation sites under tensile loading.
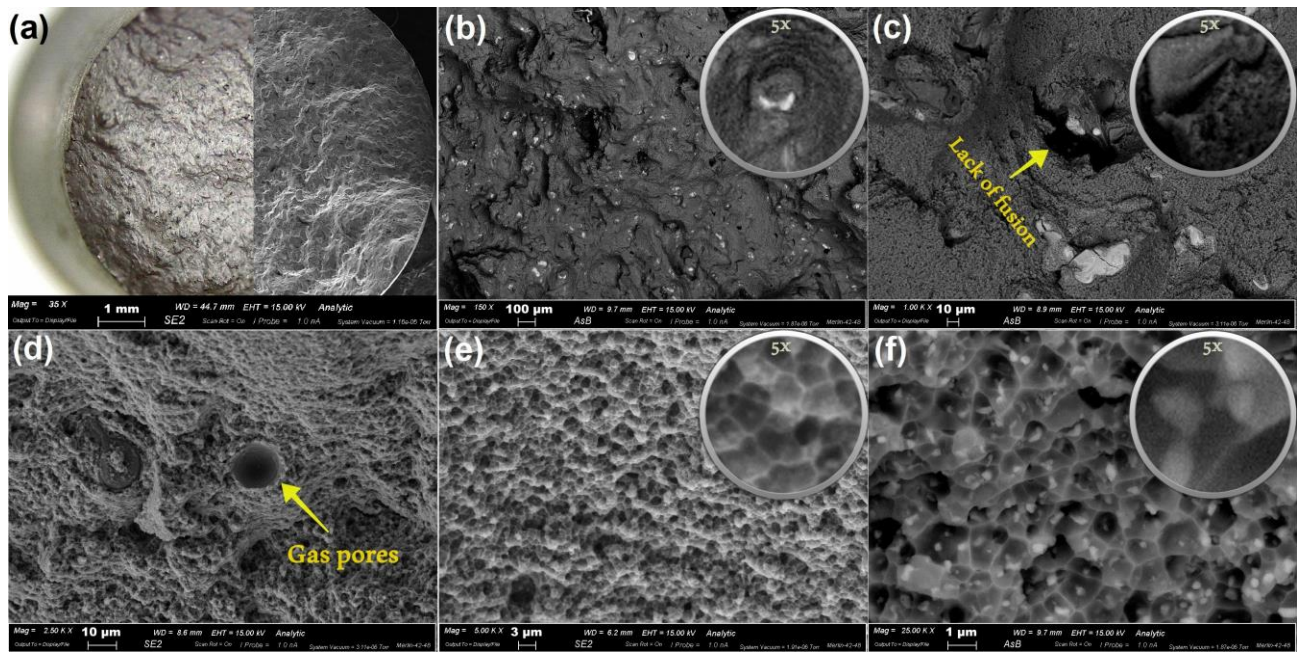
**Fig. 14**. Stere/SEM (a) and SEM images were provided from the fracture surface of the as-built sample (b, c) after annealing at 300 °C for 120 min (d-f).

### 3.2. Mechanical properties

To evaluate the effect of short-term and long-term annealing on the mechanical performance of the AlSi10Mg/Ni samples, tensile and compression tests were executed, and the results are presented in **Fig. 15**. According to **Fig. 15(a),** annealing at 300 °C for 15 min could not significantly attenuate the compressive yield strength, even if it is evident that the as-built samples break in a brittle fashion, while the treated samples (in particular the one annealed for 120 min) have a more ductile behaviour. In fact, to keep on the annealing up to 120 min has remarkably reduced the compressive yield strength, from about 330 MPa to near 220 MPa. According to the tensile stress-strain curves of **Fig. 15(b)**, dissociation of the silicon branches into fine particles after short-term annealing could not remarkably reduce the tensile strength of the samples. But after annealing for 2 hours, coarsening of the silicon particles played a destructive role and degraded the tensile properties. In **Fig. 15(c)**, the tensile behaviour of the AlSi10Mg/Ni samples after short- and long-term annealing is compared by AlSi10Mg alloy in a pure state and after reinforcing with different metallic and non-metallic reinforcements. As illustrated, compared to the non-reinforced AlSi10Mg, Ni-reinforced alloy shows lower tensile strength and a lower elongation to failure. Although short-term annealing could not majorly attenuate the tensile resistance, the synergistic effect

of spheroidized silicon particles and promotion of brittle $Al_3Ni$ shell around the Ni-rich lumps after annealing for 120 min resulted in a notable collapse in the mechanical properties. Furthermore, as shown, Cu-reinforced AlSiMg alloy [43] has also shown a similar tensile behaviour and rather lower strength compared to the average strength of the 3D printed AlSi10Mg alloy. The noticeable point is that according to the extracted results in the literature (Table. 2), compared to metallic elements, improvement of the mechanical strength of AlSi10Mg alloy through the addition of ceramic nanoparticles and carbon allotropes was more favorable. This suggests that to achieve a finer cell structure in the AlSi10Mg components manufactured through the LPBF process, the addition of pre-synthesized fine ceramic particles is more effective than the addition of alloying elements. In fact, the high solidification rate of the molten tracks hinders the long-range diffusion of the solute elements, and for the complete dissolution of the additive metallic particles, they must be very fine. Otherwise, applying an insufficient laser power for dissolving a couple of the particles having a significant difference in melting point (like Ni particles in Al matrix) only according to the optimum parameters for LPBF fabrication of a component cannot properly spread the guest elements among the host matrix. On the other side, exposure of the powder bed to intensive laser irradiation can lead to the formation of some pores due to the Marangoni effect [44] and vaporization of some particles of the low-melting-point ingredient.
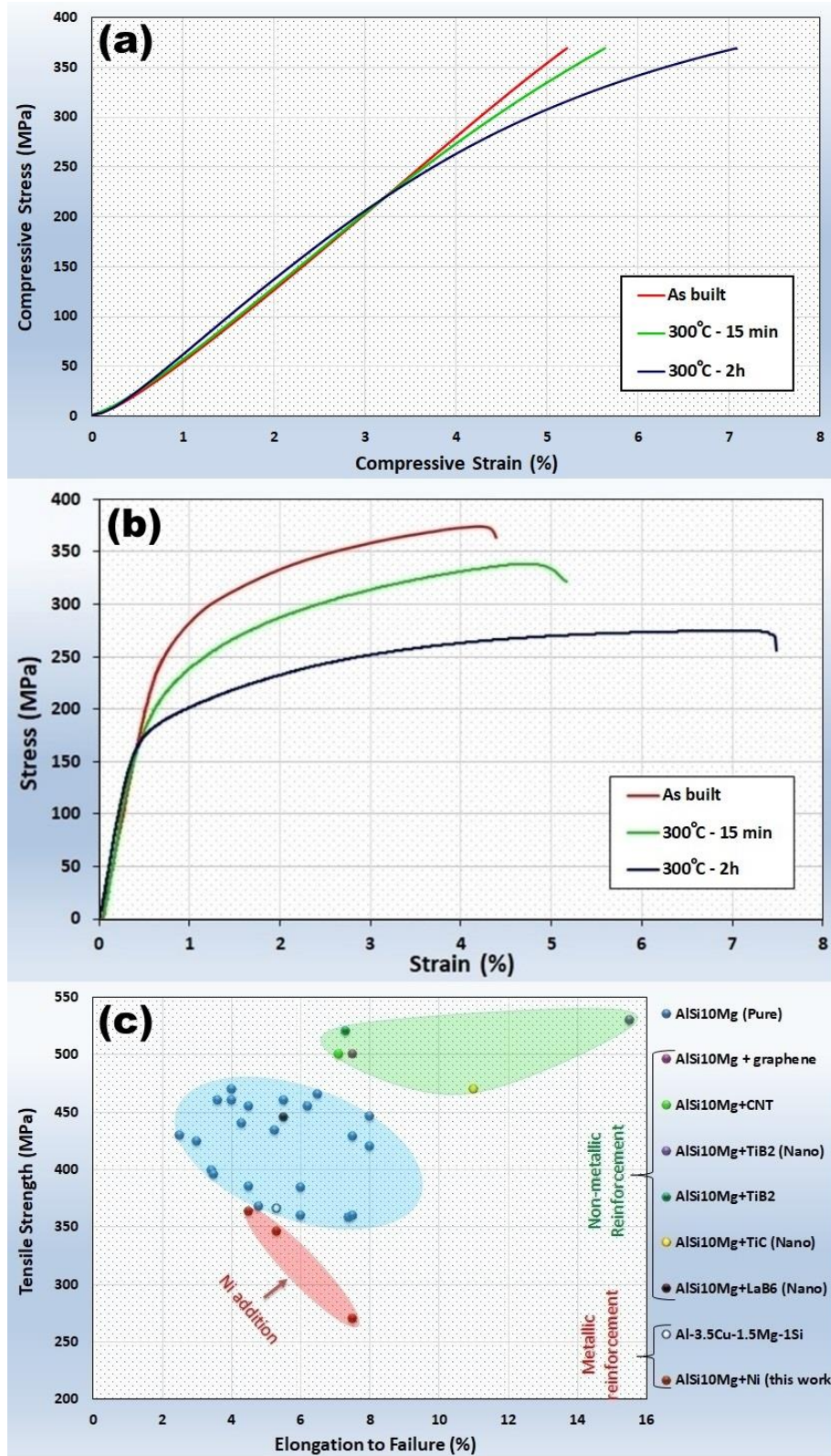
**Fig. 15**. Variation of compressive (a) and tensile (b) stress-strain curves and comparison of tensile behavior of Ni-reinforced AlSi10Mg alloy after annealing at 300 °C for 15min and 120 min with pure AlSi10Mg and reinforced alloys/composites by other additive agents (c).

**Table 2.** Overview of tensile properties of AlSi10Mg alloys reinforced by different reinforcements.

| Source | Matrix | Reinforcement material | Particle size matrix/reinforcement (µm) | Additive fraction (Wt.%) | Beam diameter (µm) | Laser power (W) | Hatching distance (µm) | Layer thickness (µm) | Scan speed (mm/s) | UTS (MPa) | El. at break (%) |
|---|---|---|---|---|---|---|---|---|---|---|---|
| This work | AlSi10Mg | Ni | <45/<20 | 5 | 100 | 195 | 170 | 30 | 800 | 270-370 | 4.4-7.5 |
| [23] | AlSi10Mg | TiC | 30/1.5 | 5 | 70 | 100 | 50 | 50 | 150 | 470 | 11 |
| [19] | AlSi10Mg | $TiB_2$ | 53/15 | 5.6 | 75 | 210 | 100 | 30 | 1000 | 520 | 7.3 |
| [45] | AlSi10Mg | Nano-$TiB_2$ | <40/nano-sized | 11.6 | 75 | 300 | 105 | 30 | 1000 | 530 | 15.5 |
| [16] | AlSi10Mg | $LaB_6$ | 40/100 nm | 0.5 | 70-100 | 300 | 130 | 30 | 1650 | 445 | 5.5 |
| [46] | AlSi10Mg | Graphene | 15-45/- | 0.1-0.2 | 73 | 400 | 90 | 30 | 2250 | 500 | 7.5 |
| [43] | AlSiMg | Cu | 41 | 3.5 | 70-250 | 190 | 80 | 40 | 165 | 366 | 5.3 |
| [22] | AlSi10Mg | CNT | <45/10-30 nm | 1 | 70-500 | 370 | 105 | 30 | 1300 | 500 | 7.1 |
| [1, 12, 38, 43, 47-58] | AlSi10Mg (Pure) | - | - | - | - | - | - | - | - | 358-470 | 3-8 |

## 4. Summary and conclusions

In the current study, the AlSi10Mg powder was combined with 5 wt.% gas atomized powder of pure Ni and then processed using the LPBF additive manufacturing method. Samples were eventually annealed at 300 °C for different times, and their microstructure and mechanical properties were surveyed. The main achievements of this research are summarized as follows:

- ❖ The as-built sample had a fish-scale pattern in which the grains were oriented from the center toward the borders of the melt pools. After annealing the samples at 300 °C for 15min, both the GBs and melt pools were gradually faded while keeping on the annealing for 120 min resulted in the complete disappearance of the melt pools.

- ❖ During the printing process, most of the Ni particles reacted with the Al matrix and formed $Al_3Ni$ phase and shoved towards the bottom of the melt pools and located there. During annealing, the cellular dendritic structure formed in the as-built sample gradually spheroidized into fine (after 15 min) and coarse (after 120 min) silicon particles, but the Ni-rich zones did not majorly affect from annealing and preserved their initial positions.

❖ Microstructural investigation revealed that the high tendency of the Ni particles to accumulation stimulated them to form coarse Ni-rich lumps in the center of the melt pools. However, annealing at 300 °C for 15 min could not majorly affect the stacked Ni-rich chunks and the residual pure Ni but after 120 min, a thick fragile shell of $Al_3Ni$ was formed on Ni-rich masses. The creation of such a brittle crust on numerous Ni-rich lumps having weak interfacial bonding with Al matrix and transformation of silicon cellular dendrites to the coarse particles with sharp edges resulted in a significant drop in tensile strength and a slight reduction in compressive resistance after long-term annealing.

❖ Comparison of the tensile strength of the AlSi10Mg/Ni alloy with tensile behaviour of the AlSi10Mg alloy and reinforced alloys by other materials revealed that compared to metallic elements, the addition of ceramic nanoparticles and carbon nano-compounds has a higher impact on the improvement of mechanical properties.

# References

[1] W.H. Kan, Y. Nadot, M. Foley, L. Ridosz, G. Proust, J.M. Cairney, Factors that affect the properties of additively-manufactured AlSi10Mg: Porosity versus microstructure, Additive Manufacturing 29 (2019) 100805.

[2] M.R. Jandaghi, A. Saboori, L. Iuliano, M. Pavese, On the effect of rapid annealing on the microstructure and mechanical behavior of additively manufactured stainless steel by Laser Powder Bed Fusion, Materials Science and Engineering: A (2021) 142109.

[3] T. Hirata, T. Kimura, T. Nakamoto, Effects of hot isostatic pressing and internal porosity on the performance of selective laser melted AlSi10Mg alloys, Materials Science and Engineering: A 772 (2020) 138713.

[4] D. Dai, D. Gu, Influence of thermodynamics within molten pool on migration and distribution state of reinforcement during selective laser melting of AlN/AlSi10Mg composites, International Journal of Machine Tools and Manufacture 100 (2016) 14-24.

[5] J. Delahaye, J.T. Tchuindjang, J. Lecomte-Beckers, O. Rigo, A. Habraken, A. Mertens, Influence of Si precipitates on fracture mechanisms of AlSi10Mg parts processed by Selective Laser Melting, Acta Materialia 175 (2019) 160-170.

[6] T.-H. Park, M.-S. Baek, H. Hyer, Y. Sohn, K.-A. Lee, Effect of direct aging on the microstructure and tensile properties of AlSi10Mg alloy manufactured by selective laser melting process, Materials Characterization 176 (2021) 111113.

[7] X. Liu, C. Zhao, X. Zhou, Z. Shen, W. Liu, Microstructure of selective laser melted AlSi10Mg alloy, Materials & Design 168 (2019) 107677.

[8] A. Hadadzadeh, B.S. Amirkhiz, A. Odeshi, J. Li, M. Mohammadi, Role of hierarchical microstructure of additively manufactured AlSi10Mg on dynamic loading behavior, Additive Manufacturing 28 (2019) 1-13.

[9] V. Fallah, A. Korinek, B. Raeisinia, M. Gallerneault, S. Esmaeili, Early-stage precipitation phenomena and composition-dependent hardening in Al-Mg-Si-(Cu) alloys, Mater. Sci. Forum, Trans Tech Publ, 2014, pp. 933-938.

[10] A.H. Maamoun, M. Elbestawi, G.K. Dosbaeva, S.C. Veldhuis, Thermal post-processing of AlSi10Mg parts produced by Selective Laser Melting using recycled powder, Additive Manufacturing 21 (2018) 234-247.

[11] N.T. Aboulkhair, I. Maskery, C. Tuck, I. Ashcroft, N.M. Everitt, Improving the fatigue behaviour of a selectively laser melted aluminium alloy: Influence of heat treatment and surface quality, Materials & Design 104 (2016) 174-182.

[12] W. Li, S. Li, J. Liu, A. Zhang, Y. Zhou, Q. Wei, C. Yan, Y. Shi, Effect of heat treatment on AlSi10Mg alloy fabricated by selective laser melting: Microstructure evolution, mechanical properties and fracture mechanism, Materials Science and Engineering: A 663 (2016) 116-125.

[13] L. Zhou, A. Mehta, E. Schulz, B. McWilliams, K. Cho, Y. Sohn, Microstructure, precipitates and hardness of selectively laser melted AlSi10Mg alloy before and after heat treatment, Materials Characterization 143 (2018) 5-17.

[14] M.R. Jandaghi, H. Pouraliakbar, A. Saboori, Effect of second-phase particles evolution and lattice transformations while ultrafine graining and annealing on the corrosion resistance and electrical conductivity of Al–Mn–Si alloy, Materials Research Express 6(10) (2019) 1065d9.

[15] T. Kimura, T. Nakamoto, Microstructures and mechanical properties of A356 (AlSi7Mg0. 3) aluminum alloy fabricated by selective laser melting, Materials & Design 89 (2016) 1294-1301.

[16] Q. Tan, J. Zhang, N. Mo, Z. Fan, Y. Yin, M. Bermingham, Y. Liu, H. Huang, M.-X. Zhang, A novel method to 3D-print fine-grained AlSi10Mg alloy with isotropic properties via inoculation with LaB6 nanoparticles, Additive Manufacturing 32 (2020) 101034.

[17] A.S. Konopatsky, D.G. Kvashnin, S. Corthay, I. Boyarintsev, K.L. Firestein, A. Orekhov, N. Arkharova, D.V. Golberg, D.V. Shtansky, Microstructure evolution during AlSi10Mg molten alloy/BN microflake interactions in metal matrix composites obtained through 3D printing, Journal of Alloys and Compounds 859 (2021) 157765.

[18] Y. Chen, S. Song, S. Zhu, X. Cui, F. Zhao, Selective laser remelting of in-situ Al2O3 particles reinforced AlSi10Mg matrix composite: Densification, microstructure and microhardness, Vacuum (2021) 110365.

[19] Y. Xiao, Z. Bian, Y. Wu, G. Ji, Y. Li, M. Li, Q. Lian, Z. Chen, A. Addad, H. Wang, Effect of nano-TiB2 particles on the anisotropy in an AlSi10Mg alloy processed by selective laser melting, Journal of Alloys and Compounds 798 (2019) 644-655.

[20] M.L. Montero-Sistiaga, M. Godino-Martinez, K. Boschmans, J.-P. Kruth, J. Van Humbeeck, K. Vanmeensel, Microstructure evolution of 316L produced by HP-SLM (high power selective laser melting), Additive Manufacturing 23 (2018) 402-410.

[21] Z. Zhao, P. Bai, R. Misra, M. Dong, R. Guan, Y. Li, J. Zhang, L. Tan, J. Gao, T. Ding, AlSi10Mg alloy nanocomposites reinforced with aluminum-coated graphene: selective laser melting, interfacial microstructure and property analysis, Journal of Alloys and Compounds 792 (2019) 203-214.

[22] L. Jiang, T. Liu, C. Zhang, K. Zhang, M. Li, T. Ma, W. Liao, Preparation and mechanical properties of CNTs-AlSi10Mg composite fabricated via selective laser melting, Materials Science and Engineering: A 734 (2018) 171-177.

[23] H. Wang, D. Gu, Nanometric TiC reinforced AlSi10Mg nanocomposites: Powder preparation by high-energy ball milling and consolidation by selective laser melting, J. Compos. Mater. 49(13) (2015) 1639-1651.

[24] C. Li, S. Sun, Y. Zhang, C. Liu, P. Deng, M. Zeng, F. Wang, P. Ma, W. Li, Y. Wang, Effects of laser processing parameters on microstructure and mechanical properties of additively manufactured AlSi10Mg alloys reinforced by TiC, The International Journal of Advanced Manufacturing Technology 103(5) (2019) 3235-3246.

[25] T.B. Sercombe, X. Li, Selective laser melting of aluminium and aluminium metal matrix composites, Materials Technology 31(2) (2016) 77-85.

[26] P. Rometsch, Q. Jia, K.V. Yang, X. Wu, Aluminum alloys for selective laser melting–towards improved performance, Additive Manufacturing for the Aerospace Industry, Elsevier2019, pp. 301-325.

[27] M. Wang, B. Song, Q. Wei, Y. Zhang, Y. Shi, Effects of annealing on the microstructure and mechanical properties of selective laser melted AlSi7Mg alloy, Materials Science and Engineering: A 739 (2019) 463-472.

[28] A. Aversa, M. Lorusso, G. Cattano, D. Manfredi, F. Calignano, E.P. Ambrosio, S. Biamino, P. Fino, M. Lombardi, M. Pavese, A study of the microstructure and the mechanical properties of an AlSiNi alloy produced via selective laser melting, Journal of Alloys and Compounds 695 (2017) 1470-1478.

[29] H. Pouraliakbar, S. Firooz, M.R. Jandaghi, G. Khalaj, A. Amirafshar, Combined effect of heat treatment and rolling on pre-strained and SPDed aluminum sheet, Materials Science and Engineering: A 612 (2014) 371-379.

[30] I. ASTM, Standard test methods for tension testing of metallic materials 1, Astm.

[31] W. Pei, W. Zhengying, C. Zhen, L. Junfeng, Z. Shuzhe, D. Jun, Numerical simulation and parametric analysis of selective laser melting process of AlSi10Mg powder, Appl. Phys. A 123(8) (2017) 1-15.

[32] J. Guan, Y. Jiang, X. Zhang, X. Chong, Microstructural evolution and EBSD analysis of AlSi10Mg alloy fabricated by selective laser remelting, Materials Characterization 161 (2020) 110079.

[33] C. Liu, C. Li, Z. Zhang, S. Sun, M. Zeng, F. Wang, Y. Guo, J. Wang, Modeling of thermal behavior and microstructure evolution during laser cladding of AlSi10Mg alloys, Optics & Laser Technology 123 (2020) 105926.

[34] M.R. Jandaghi, H. Pouraliakbar, A. Saboori, S.I. Hong, M. Pavese, Comparative Insight into the Interfacial Phase Evolutions during Solution Treatment of Dissimilar Friction Stir Welded AA2198-AA7475 and AA2198-AA6013 Aluminum Sheets, Materials 14(5) (2021) 1290.

[35] M.R. Jandaghi, H. Pouraliakbar, S.I. Hong, M. Pavese, Grain boundary transition associated intergranular failure analysis at TMAZ/SZ interface of dissimilar AA7475-AA2198 joints by friction stir welding, Materials Letters 280 (2020) 128557.

[36] E. Rabkin, L.S. Shvindlerman, B.B. Straumal, Grain boundaries: phase transitions and critical phenomena, International Journal of Modern Physics B 5(19) (1991) 2989-3028.

[37] B. Straumal, O. Kogtenkova, P. Zięba, Wetting transition of grain-boundary triple junctions, Acta materialia 56(5) (2008) 925-933.

[38] A. Kempf, K. Hilgenberg, Influence of sub-cell structure on the mechanical properties of AlSi10Mg manufactured by laser powder bed fusion, Materials Science and Engineering: A 776 (2020) 138976.

[39] F. Alghamdi, X. Song, A. Hadadzadeh, B. Shalchi-Amirkhiz, M. Mohammadi, M. Haghshenas, Post heat treatment of additive manufactured AlSi10Mg: On silicon morphology, texture and small-scale properties, Materials Science and Engineering: A 783 (2020) 139296.

[40] P. Yang, M.A. Rodriguez, L.A. Deibler, B.H. Jared, J. Griego, A. Kilgo, A. Allen, D.K. Stefan, Effect of thermal annealing on microstructure evolution and mechanical behavior of an additive manufactured AlSi10Mg part, J. Mater. Res. 33(12) (2018) 1701-1712.

[41] T. Maconachie, M. Leary, J. Zhang, A. Medvedev, A. Sarker, D. Ruan, G. Lu, O. Faruque, M. Brandt, Effect of build orientation on the quasi-static and dynamic response of SLM AlSi10Mg, Materials Science and Engineering: A 788 (2020) 139445.

[42] T. Wang, S. Dai, H. Liao, H. Zhu, Pores and the formation mechanisms of SLMed AlSi10Mg, Rapid Prototyping Journal (2020).

[43] P. Wang, C. Gammer, F. Brenne, K.G. Prashanth, R.G. Mendes, M.H. Rümmeli, T. Gemming, J. Eckert, S. Scudino, Microstructure and mechanical properties of a heat-treatable Al-3.5 Cu-1.5 Mg-1Si alloy produced by selective laser melting, Materials Science and Engineering: A 711 (2018) 562-570.

[44] S.A. Khairallah, A.T. Anderson, A. Rubenchik, W.E. King, Laser powder-bed fusion additive manufacturing: Physics of complex melt flow and formation mechanisms of pores, spatter, and denudation zones, Acta Materialia 108 (2016) 36-45.

[45] X.P. Li, G. Ji, Z. Chen, A. Addad, Y. Wu, H. Wang, J. Vleugels, J. Van Humbeeck, J.-P. Kruth, Selective laser melting of nano-TiB2 decorated AlSi10Mg alloy with high fracture strength and ductility, Acta Materialia 129 (2017) 183-193.

[46] A. Mandal, J.K. Tiwari, N. Sathish, A.K. Srivastava, Microstructural and mechanical properties evaluation of graphene reinforced stainless steel composite produced via selective laser melting, Materials Science and Engineering: A (2020) 138936.

[47] S.R. Ch, A. Raja, P. Nadig, R. Jayaganthan, N. Vasa, Influence of working environment and built orientation on the tensile properties of selective laser melted AlSi10Mg alloy, Materials Science and Engineering: A 750 (2019) 141-151.

[48] Y. Bai, Y. Yang, Z. Xiao, M. Zhang, D. Wang, Process optimization and mechanical property evolution of AlSiMg0. 75 by selective laser melting, Materials & Design 140 (2018) 257-266.

[49] K. Kempen, L. Thijs, J. Van Humbeeck, J.-P. Kruth, Processing AlSi10Mg by selective laser melting: parameter optimisation and material characterisation, Materials Science and Technology 31(8) (2015) 917-923.

[50] C. Zhang, H. Zhu, H. Liao, Y. Cheng, Z. Hu, X. Zeng, Effect of heat treatments on fatigue property of selective laser melting AlSi10Mg, Int. J. Fatigue 116 (2018) 513-522.

[51] D. Knoop, A. Lutz, B. Mais, A. von Hehl, A tailored AlSiMg alloy for laser powder bed fusion, Metals 10(4) (2020) 514.

[52] G. Qian, Z. Jian, Y. Qian, X. Pan, X. Ma, Y. Hong, Very-high-cycle fatigue behavior of AlSi10Mg manufactured by selective laser melting: Effect of build orientation and mean stress, Int. J. Fatigue 138 (2020) 105696.

[53] N. Takata, H. Kodaira, K. Sekizawa, A. Suzuki, M. Kobashi, Change in microstructure of selectively laser melted AlSi10Mg alloy with heat treatments, Materials Science and Engineering: A 704 (2017) 218-228.

[54] P. Wei, Z. Wei, Z. Chen, J. Du, Y. He, J. Li, Y. Zhou, The AlSi10Mg samples produced by selective laser melting: single track, densification, microstructure and mechanical behavior, Applied surface science 408 (2017) 38-50.

[55] N.E. Uzan, R. Shneck, O. Yeheskel, N. Frage, Fatigue of AlSi10Mg specimens fabricated by additive manufacturing selective laser melting (AM-SLM), Materials Science and Engineering: A 704 (2017) 229-237.

[56] Z. Li, Z. Li, Z. Tan, D.-B. Xiong, Q. Guo, Stress relaxation and the cellular structure-dependence of plastic deformation in additively manufactured AlSi10Mg alloys, International Journal of Plasticity 127 (2020) 102640.

[57] S. Zhou, Y. Su, R. Gu, Z. Wang, Y. Zhou, Q. Ma, M. Yan, Impacts of defocusing amount and molten pool boundaries on mechanical properties and microstructure of selective laser melted AlSi10Mg, Materials 12(1) (2019) 73.

[58] L. Zhuo, Z. Wang, H. Zhang, E. Yin, Y. Wang, T. Xu, C. Li, Effect of post-process heat treatment on microstructure and properties of selective laser melted AlSi10Mg alloy, Materials Letters 234 (2019) 196-200.